Title

Evaluation of Hamamatsu PET Imaging Modules for Dedicated TOF-Capable Scanners

Permalink

https://escholarship.org/uc/item/37j3q4jq

Journal

IEEE Transactions on Radiation and Plasma Medical Sciences, 3(6)

ISSN

2469-7311

Authors

Stolin, A
Jaliparthi, G
Raylman, RR
et al.

Publication Date

2019-11-01

DOI

10.1109/trpms.2019.2894974

Peer reviewed

Evaluation of Hamamatsu PET imaging modules for dedicated TOF-capable scanners

A. Stolin[1], **G. Jaliparthi**[1], **R.R. Raylman**[1], **J. Brefczynski-Lewis**[1], **S. Majewski**[2], **J. Qi**[3], **K. Gong**[3], **S. Dolinsky**[4]

[1]Center for Advanced Imaging, Department of Radiology, West Virginia University, Morgantown, WV

[2]Department of Radiology, University of Virginia, Charlottesville, VA

[3]Department of Nuclear Medicine, UC-Davis, Davis, CA

[4]GE-GRC, Niskayuna, NY

Abstract

Time-of-flight (TOF) capability is becoming an important capability offered in both commercial and research PET scanners. Often commercial vendors and laboratory researchers develop and utilize proprietary electronics for their devices. Consequently, it is challenging for independent research groups to develop their own TOF-PET scanners. In this investigation, we tested a prototype scanner consisting of commercially available TOF-capable modules from Hamamatsu Photonics that can be used as building blocks for PET scanners. The scanner consists of a ring of 16 modules, for a total diameter of 26.7 cm. Testing demonstrated that the scanner is capable of sustaining ~1 MHz single counting rate with a peak noise equivalent count rate (NECR) of 117.5 kHz at 75.25 MBq measured with NEMA NU-4 "rat" phantom. Spatial resolution of 2.3 mm 5 mm from the center of the scanner was measured. Energy resolution of 17.2% at 511 keV was measured. Peak sensitivity of 1.28% is reported. All the measurements were performed with energy cuts from 350 to 700 keV Finally, scanner timing resolution was found to be 462 ps. Results from testing of a prototype scanner constructed using newly released TOF-capable detector modules produced by Hamamatsu demonstrated the promise for these devices to create high performance PET system with TOF capabilities.

Keywords

PET Instrumentation; Nuclear Medicine Imaging; SiPM; TOF

I.   Introduction

Time-of-flight (TOF) resolution on the order of several hundreds of picoseconds is becoming an essential capability for high performance PET imaging. First proposed nearly 40 years ago [1–3], TOF utilizes the difference between accurately measured arrival times of

annihilation photons to estimate the positions of positron annihilations. Despite initial success, further progress on TOF-capable scanners was achieved only some 20 years later with the introduction of faster and brighter scintillators [4–6]. Development of high-gain semiconductor low-level light sensors, silicon photomultipliers (SiPMs), also contributed to the rapid adoption of TOF techniques to PET imaging [7–10]. TOF has the potential to improve signal-to-noise ratio, improve spatial resolution and decrease the radiation dose and/or scan time compared to non-TOF scanners [11–15].

Currently, individual research groups only gain access to TOF technology by purchasing scanners from commercial vendors or by undertaking costly development programs to create their own hardware [16–20]. To address this lack of access to TOF technology, Hamamatsu Photonics (HPK) recently brought to market a line of complete TOF-capable imaging modules [21]. These devices can be customized with different scintillation arrays, offering pixel sizes from 1.5 to 4 mm. They can be daisy-chained with common timing and data transfer lines, allowing construction of custom TOF-PET scanners. The aim of this study is to evaluate the ability of new, commercially available TOF-capable detector modules to create a small PET system. Specifically, we assessed the performance of a prototype, small diameter PET scanner constructed from the modules.

II. Methods

A. Apparatus description

Each HPK module (C13500–4075LC-12) contains a 12×12 array of 4.1×4.1×20 mm LFS scintillator elements (4.205 mm pixel pitch) individually coupled to a 12×12 array of multi-pixel photon counters (MPPCs). The total detection area is ~50×50 mm^2. The modules are hermetically sealed to make them light and air tight. The MPPC array is read out with two digital boards. Each board contains an array of four application-specific integrated circuits (ASIC). Each ASIC digitizes 18 analog channels, providing information about event position, energy and timing. Energy estimation is implemented as time-over-threshold (ToT) with resolution of 4 ns. Event timing is provided by a timestamp, common for all the channels served by an ASIC. A module is housed in an aluminum casing to provide mechanical robustness and light weight. Individual modules were mounted inside 3D-printed plastic holders. Fans were included inside the housing to cool the electronics. Each complete detector module weighs approximately 0.5 kg.

16 detector units were daisy-chained and arranged in a ring geometry with a diameter of 26.7 cm and axial coverage of ~5 cm. A Korad KA3305P multi-channel power supply was used to provide power to the modules and control electronic boards. Electronics include two power supply boards, three timing distribution boards and a data relay board. A relay board receives data from the modules and sends it to a host PC via an optical data link. A 10 MHz timing signal was generated internally by the data relay board and distributed through the master timing board to slave timing boards and, ultimately, to the detector modules. Fig.1 shows the connection of two modules. Fig. 2 shows the complete prototype scanner using 16 modules.

Data acquisition was coordinated by connecting the module electronics shown in Fig. 1 to a Dell Optiplex workstation (i7 processor, 32 Gb of RAM) running Windows 7 Professional OS. Hamamatsu proprietary data acquisition software version 1.0.8.1, written in C#, was utilized to acquire raw data from the scanner. Our revision of the firmware supported 16-bytes per event data format. Event data in such format are reported only for the highest energy channel, thus estimation of light sharing and inter-crystal Compton scatter was not possible.

The system does not possess external triggering capabilities. Thus, the software stores singles data from all the detectors to a hard drive. These data are then accessed by Java-based, custom software that determines coincidence events and converts the data to list-mode data for further processing and reconstruction. The system provides a timing step of 15.625 ps, allowing for a narrow timing window for better rejection of random events. After some experimentation, we chose to utilize 1 ns window.

B. Calibration and preliminary measurements

Energy calibration of the system was performed with ^{22}Na and ^{137}Cs sources, as well as 202 and 307 keV lines of ^{176}Lu using the formalism described in [24]. Timing correction was performed by rotating a line source filled with ^{18}F placed outside the useful field of view (12.5 cm away from the center). The source was rotated at an angular speed of 1 degree/ second and measurements were repeated 5 times with source activities around 250 μCi. Timing spectra were obtained for each line-of-response (LOR) and their centers were calculated by fitting the timing distributions to a Gaussian function. Locations of the line source were calculated using angular velocity and data timestamps. Timing calibration offsets were calculated as the differences between the centers of the timing spectra and predictions for each LOR based on the location of the radioactive line source. Assessment of the sustainable count rate was performed by placing a 74 MBq ^{18}F source at various distances from the detectors faces.

C. NEMA NU-4-based evaluations

The basic performance characteristics of the scanner were assessed using the NEMA NU4–2008 protocol. Specifically, spatial resolution was measured by stepping a point source of ^{22}Na (50μCi) mounted in a 1cm^3 block of acrylic to several radial positions at two axial positions: center of the scanner and 12 mm (1/4 of the FOV) away from the center. Images were reconstructed using filtered back projection (FBP) and maximum likelihood expectation minimization (MLEM) iterated until a stable point source width was obtained (15 iterations)) reconstruction algorithms. The full width-at-half-maximum (FWHM) of intensity profiles acquired from images of the point source are reported as spatial resolution. Detection sensitivity was measured by stepping the same point source to 28 positions along the central axis of the scanner. These data were used to calculate detection sensitivity at each location. Throughout system assessment we utilized an energy window of 350 to 700 keV. Noise equivalent counting rate (NECR) was measured using the "rat-like" phantom with a starting activity of 96 MBq of ^{18}F. Random and scattered events were estimated, as per NEMA NU-2008 standard, by measuring total and combined scatter and random rates from data acquired as the source decays. The intrinsic coincidence rate due to the presence of

^{176}Lu was evaluated with no source in the field of view. These data are used to estimate true coincidence rates. Scatter fraction was estimated using low activity data points, where random rates are negligible. Finally, image uniformity and spillover ratios were measured from MLEM-reconstructed images of the phantom.

D. Timing resolution measurements and phantom imaging

To measure the system's timing resolution, a 70 μCi ^{18}F line source was placed at the center of the scanner. A data set containing approximately 100 million total events was then acquired. Timing calibration offsets were applied and an overall timing spectrum was fit to a Gauss function. FWHM of the fit is reported as timing resolution. Finally, reconstructed images of a mini-hot-rod phantom with rod diameters of 1.2, 1.6, 2.4, 3.2, 4 and 4.8 mm and the Hoffman brain phantom were obtained with and without timing information for comparison. They were filled with ^{18}F solution with activities of 3.7 and 5.6 MBq respectively. Data were acquired for 5 minutes. An energy threshold window of 350 to 700 keV and 1 ns gate time were applied in post-processing. Phantom data were reconstructed using the MLEM reconstruction algorithm [22] with modeled attenuation corrections based on knowledge of the phantom's photon attenuation characteristics.

III.   Results

A.   Energy resolution and counting rate

A single pixel energy spectra obtained with a ^{22}Na source before and after linearization are shown in Fig.3 a) and b). After calibration, the overall energy resolution of the scanner is 17.2 % FWHM. Average energy resolution over all the crystals was 16.9 ± 2.7% (range 13.7% to 17.9%). The single-detector maximum-counting rate is 968 kHz.

B.   NEMA NU-4-based evaluations

Fig. 4a) and b) show plots of spatial resolution as a function of the source's trans-axial displacement from the center of the scanner. A strong discrepancy can be noted between 2.3 mm resulting from MLEM reconstruction and 6.1 mm obtained with FBP. Fig. 5 shows a plot of detection sensitivity measured with energy window of 350 to 700 keV. Peak sensitivity is 1.27%.

Results from measurement of count rate capability are shown in Fig. 6. Peak NECR is 117.5 kcps at 75.25 MBq. The average counting rate of individual modules is 968 kcps, which agrees well with the ~1 MHz specified by the manufacturer. A sharp drop in counting rate at high activity levels is attributed to partial shutdown of bias voltage, which is a safety mechanism implemented by the manufacturer to protect the detector electronics from current spikes.

Fig. 7 displays single slices of the non-TOF-corrected images of the NEMA quality assurance phantom. Analysis of the uniformity section of the QA phantom produced a value of 18.2+/−1.18 %. Spillover ratios are 17% and 23% for the air and water filled areas, respectively. Finally, contrast recovery coefficients were measured to be 0.65, 0.42, 0.26, 0.10 and 0 for 5, 4, 3, 2, and 1 mm-diameter rods, respectively.

C. Timing resolution

While single pixel timing resolutions were within manufacturer's specifications of ~300 ps, system timing resolution, however, is 462 ps FWHM. The difference in timing resolution between single pixel and system configurations is likely due to time jitter introduced by daisy-chaining the modules.

D. Phantom imaging

Slices of reconstructed volumes of mini-hot-rod and Hoffman brain phantoms are shown in Figs. 9 and 10. The 3.2 mm-diameter rods are clearly resolved. Incorporation of time-of-flight information in the image reconstruction process improved, slightly, the ability to resolve the smaller rods. Images of the Hoffman brain phantom also demonstrated improvement in the ability to resolve small structures due to the addition of TOF information..

IV.   Discussion

The commercial availability of TOF-capable imaging modules makes this technology available to a wider range of research groups. This access may enhance creation of custom PET scanners developed by smaller groups. We demonstrated this capability by constructing a relatively small diameter PET scanner that could be used as a small animal scanner, or as an ambulatory brain-PET scanner, for example. An attractive feature of the new detector modules is the ability to utilize them to create relatively large scanners. The modules can be daisy-chained with minimal amount of wiring; eliminating noise-prone analog data transfer. The timing distribution board can also be arranged into a single timing source configuration, supporting up to 128 detection modules. Multiple optical data links with rates of 10 Gbps per channel minimizes dead time associated with high data transfer rates.

The modules utilize the time-over-threshold method, with resolution of 4 ns, to estimate energy of the detected event. This method is prone to non-linearity [23] and requires calibration. Application of an exponential model for the shape of the detected signal [24] yielded a system energy resolution of 17.2%. This number may be further improved by fine adjustments of the threshold values for each MPPC.

The performance of the system is comparable to many small diameter PET scanners, demonstrating the utility of the new modules. For example, the system energy resolution (17.2%) is equivalent to other scanners, range of 13.7% to 25% for LYSO-based scanners [25]. The results from NEMA NU4–2008-based testing demonstrated the ability to create a high-performing, small diameter PET scanner. The relatively poor spatial resolution measured using NEMA NU-4 protocol-required FBP-reconstructed images of a point source (~6 mm FHWM) (Fig. 4a) is surprising given the small cross sectional dimensions of the detector elements (4.1×4.1 mm^2). The cause of this unexpected result is currently under investigation; it may be linked to the use of the winner-takes-all strategy used by the data acquisition electronics. To assess the magnitude of spatial resolution when an iterative reconstruction algorithm is used, resolution measurement were repeated on MLEM-reconstructed images of the point source. Average resolution of approximately 2.2 mm

FWHM 5cm from scanner center (Fig. 4b) was achieved, which is similar to the values reported for other small-diameter scanner (range=~1.7 mm to ~2.3 mm) [26].

The peak sensitivity (1.27%) (Fig. 5) is slightly higher than the MicroPET P4 (1.19%) [26], which has dimensions very close to our system. Slight decrease in sensitivity values located approximately 1 cm away from the center can be attributed to different spacing of the central crystals in the block, 4.5 mm, compared to regularly spaced 4.2 mm outer crystals. Peak NECR (117.5 kcps) (Fig. 6) measured with the "rat-like" phantom is slightly lower than the MicroPET P4 (173 kcps) [26]. Image uniformity (18.2+/−1.18 %), spillover ratio for air-filled cylinder (17%) and water-filled cylinder (23%) values (Fig. 7), respectively, are not in the range of other similar systems. These findings are due to current lack of corrections for Compton scattering.

Applying TOF for a small-diameter scanner, such as the one described in this work, will have only modest effect. This phenomenon is demonstrated by the moderate improvement to identification of small structures in images of the mini-hot rod phantom (Fig 9.) and Hoffman brain phantom (Fig. 10). Improvement was also hindered by the relatively poor system timing resolution (460 ps) (Fig. 8). Efforts to improve this phenomenon, likely due to time jitter introduced by attaching multiple modules, are currently under investigation.

V. Conclusion

In summary, we have demonstrated the ability to create a TOF-capable PET scanner utilizing newly available modules. Testing of the system revealed that its performance is similar to other systems designed for small animal imaging. And, while the size of the scanner is not large enough to definitively demonstrate the imaging advantages of ToF, the timing resolution measured for the system is comparable to other systems. The scalability of these modules facilitates construction of PET scanners of virtually any size. Thus, the introduction of these modules makes TOF capabilities available to research groups that would not normally have access to this increasingly important technology.

References

[1]. Ter-Pogossian MM, Mullani NA, Ficke DC, Markham J, Snyder DL. Photon time-of-flight-assisted positron emission tomography. J Comput Assist Tomogr. 1981;5(2):227–39. [PubMed: 6971303]

[2]. Yamamoto M, Ficke DC, Ter-Pogossian MM. Experimental assessment of the gain achieved by the utilization of time-of-flight information in a positron emission tomograph (Super PETT I). IEEE Trans Med Imaging. 1982;1(3): 187–92. doi:10.1109/TMI.1982.4307571. [PubMed: 18238274]

[3]. Budinger TF. Time-of-flight positron emission tomography: status relative to conventional PET. J Nucl Med. 1983;24(1):73–8. [PubMed: 6336778]

[4]. Moses WW, Derenzo SE. Prospects for time-of-flight PET using LSO scintillator IEEE Trans. Nuclear Sci 1999;46(3): 474–8. doi:10.1109/23.775565.

[5]. Lewellen TK. Time-of-flight PET. Semin Nucl Med. 1998;28(3):268–75. [PubMed: 9704367]

[6]. Chai BH, Ji Y. Lutetium yttrium orthosilicate single crystal scintillator detector. US Patent 920 6,921,901. 7 26, 2005.

[7]. Surti S, Kuhn A, Werner ME, Perkins AE, Kolthammer J, Karp JS. Performance of Philips Gemini TF PET/CT scanner with special consideration for its time-of-flight imaging capabilities. J Nucl Med. 2007;48(3):471–80. [PubMed: 17332626]

[8]. Karp JS, Surti S, Daube-Witherspoon ME, Muehllehner G. Benefit of time-of-flight in PET: experimental and clinical results. J Nucl Med. 2008;49(3):462–70. [PubMed: 18287269]

[9]. Jakoby BW, Bercier Y, Conti M, Casey ME, Bendriem B, Townsend DW. Physical and clinical performance of the mCT time-of-flight PET/CT scanner. Phys Med Biol. 2011;56(8):2375. [PubMed: 21427485]

[10]. Bettinardi V, Presotto L, Rapisarda E, Picchio M, Gianolli L, Gilardi MC. Physical performance of the new hybrid PET/CT Discovery-690. Med Phys. 2011;38(10):5394–411. [PubMed: 21992359]

[11]. Muehllehner G, Karp JS. Positron emission tomography. Phys Med Biol. 2006;51(13):117–37

[12]. Conti M Focus on time-of-flight PET: the benefits of improved time resolution. Eur J Nucl Med Mol Imaging. 2011;38(6):1147–57 [PubMed: 21229244]

[13]. Lois C, Jakoby BW, Long MJ, Hubner KF, Barker DW, Casey ME, et al. An assessment of the impact of incorporating time-of-flight information into clinical PET/CT imaging. J Nucl Med. 2010;51(2):237–45. [PubMed: 20080882]

[14]. Surti S, Karp JS, Popescu LM, Daube-Witherspoon ME, Werner M. Investigation of time-of-flight benefit for fully 3-D PET. IEEE Trans Med Imaging. 2006;25(5):529–38. [PubMed: 16689258]

[15]. El Fakhri G, Surti S, Trott CM, Scheuermann J, Karp JS. Improvement in lesion detection with whole-body oncologic time-of-flight PET. J Nucl Med. 2011;52(3):347–53. [PubMed: 21321265]

[16]. Burr KC, Wang G-CJ, Du H, Mann G, Balakrishnan K, Wang J, et al. A new modular and scalable detector for a time-of-flight pet scanner. In: Nuclear Science Symposium and Medical Imaging Conference (NSS/MIC), 2012 IEEE; 2012. p. 2830–834

[17]. Son JW, Yoon HS, Won JY, Kim KY, Lee MS, GB Ko, Lee JS. Development and evaluation of a proof-of-concept prototype time-of-flight PET system based on high quantum efficiency multi-anode PMTs. J Nucl Med. 2015;56(432)

[18]. Seifert S, Schaart DR. Improving the time resolution of TOF-PET detectors by double-sided readout IEEE Trans. Nuclear Sci 2015;62(1):3–11.

[19]. Frach T, Prescher G, Degenhardt C, de Gruyter R, Schmitz A, Ballizany R. The digital silicon photomultiplier—principle of operation and intrinsic detector performance. Nuclear Science Symposium Conference Record (NSS/MIC), 2009 IEEE; 2009. p. 1959–1965.

[20]. http://www.petsyselectronics.com/web/website/docs/products/product1/PETsys%20TOFPET%20ASIC%20performance-Dec2017.pdf

[21]. https://www.hamamatsu.com/resources/pdf/ssd/pet_module_kacc9009e.pdf

[22]. Smith MF, Raylman RR, PEM-PET image reconstruction in a clinically-relevant time frame, IEEE Nuclear Science Symposium Conference Record 3, 1792–1796 (2006).

[23]. Van Dam HT, Seifert S, and Schaart DR, "The statistical distribution of the number of counted scintillation photons in digital silicon photomultipliers: model and validation", Physics in Medicine and Biology, 57(15), 4885–903 (2012). [PubMed: 22796633]

[24]. Venialgo E; Lusardi N; Geraci A; O'Neill K; Gnecchi S; Jackson C; Brunner SE; Schaart DR; Charbon E, An order-statistics-inspired, fully-digital readout approach for analog SiPM arrays, 2016 IEEE Nuclear Science Symposium, Medical Imaging Conference and Room-Temperature Semiconductor Detector Workshop (NSS/MIC/RTSD), Year: 2016, Page s: 1–5

[25]. Omidvari Negar et al. "PET performance evaluation of MADPET4: a small animal PET insert for a 7 T MRI scanner", 2017 Phys. Med. Biol 62 8671 [PubMed: 28976912]

[26]. Goertzen et al. "NEMA NU 4–2008 Comparison of Preclinical PET Imaging Systems", J Nucl Med, 2012, 8; 53(8): 1300–1309 [PubMed: 22699999]
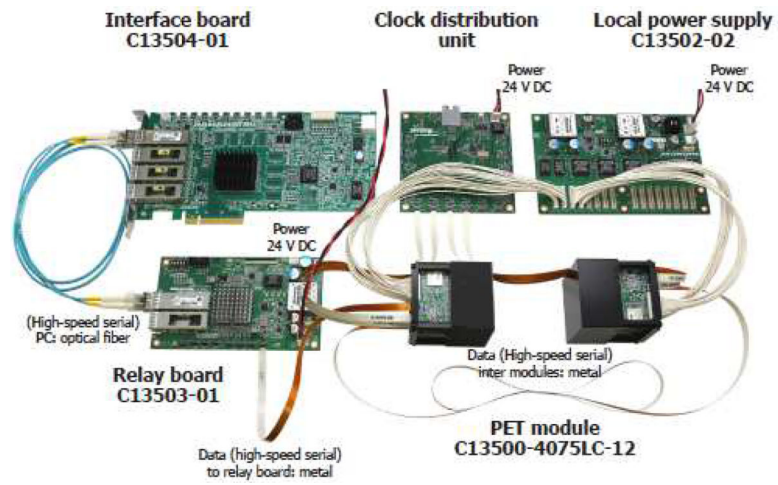
Fig. 1.
Main electronic components and two PET modules (Photo courtesy of Hamamatsu
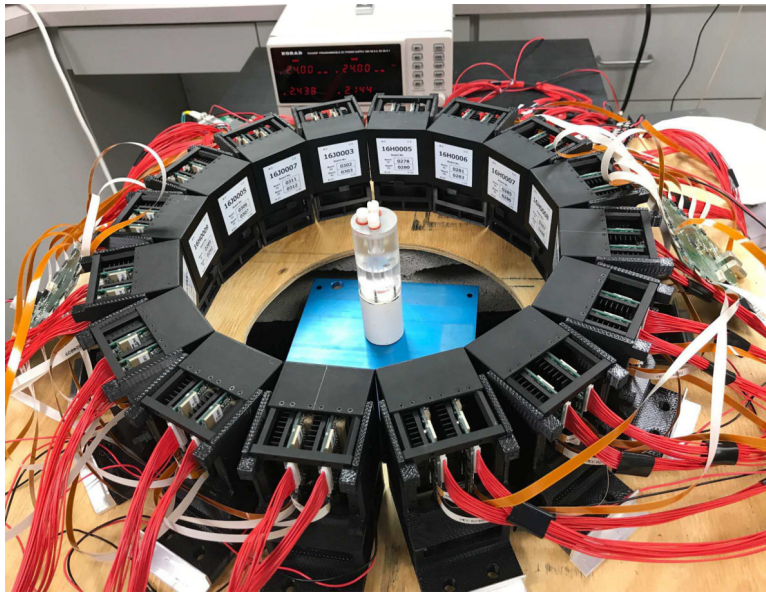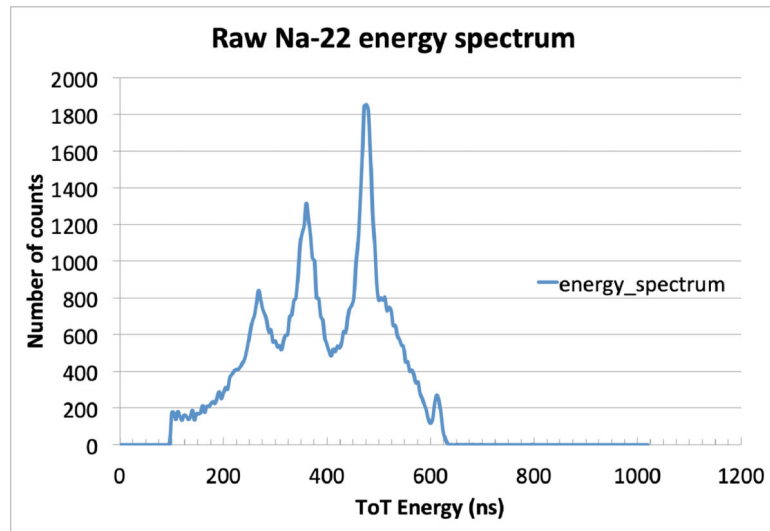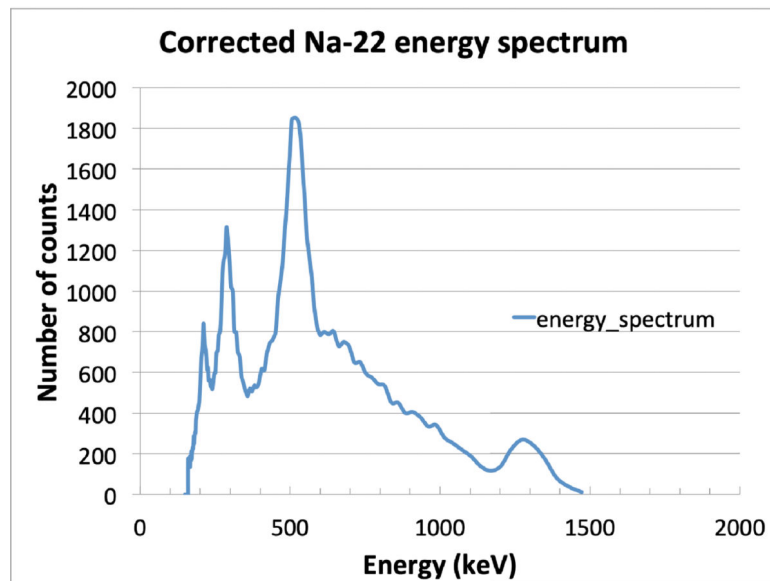Photonics Corp)

Fig. 2.
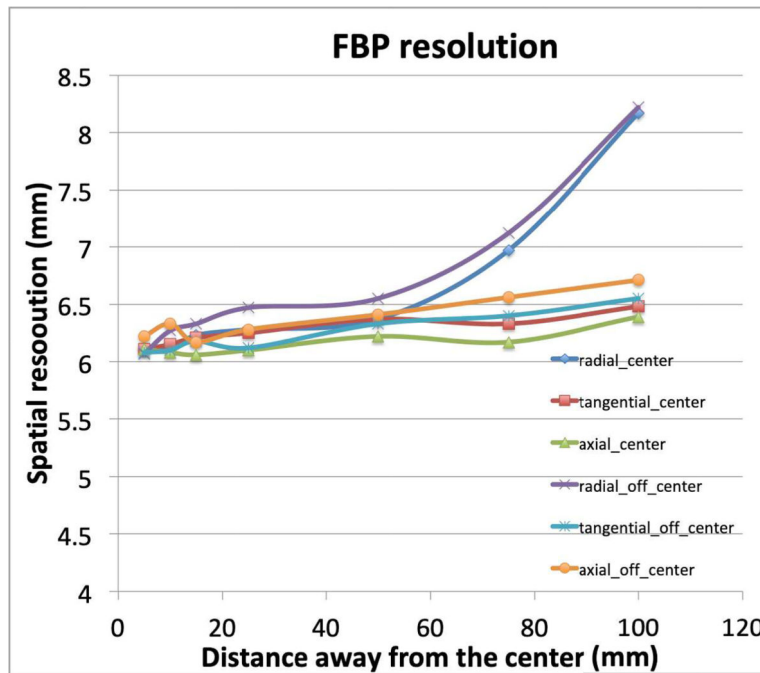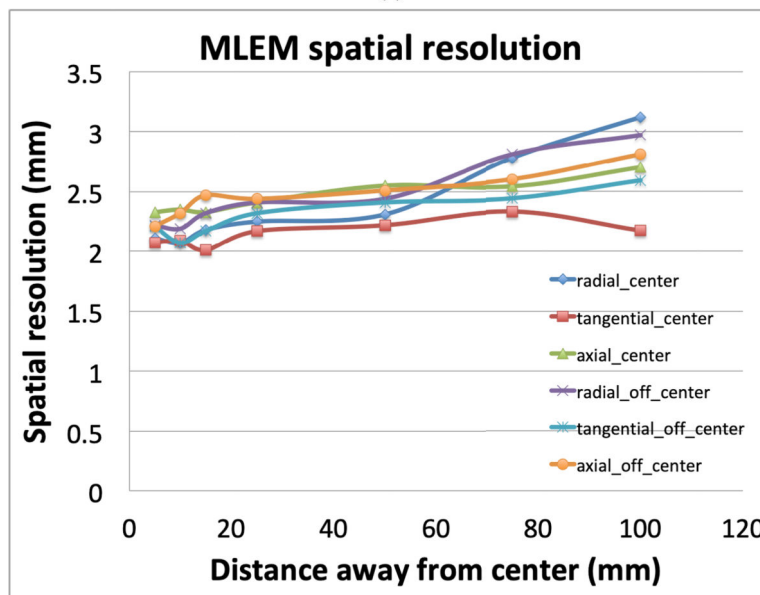Prototype PET scanner consisting of 16 modules arranged in ring geometry

(a)

(b)

Fig. 3.
(a) ^{22}Na energy spectrum acquired from a single pixel before ToT linearization (b) ^{22}Na energy spectrum acquired from a single pixel after ToT linearization

(a)

(b)

Fig. 4.
(a) Spatial resolution of the scanner obtained with FBP-reconstructed images. (b) Spatial resolution of the scanner obtained with MLEM-reconstructed images.
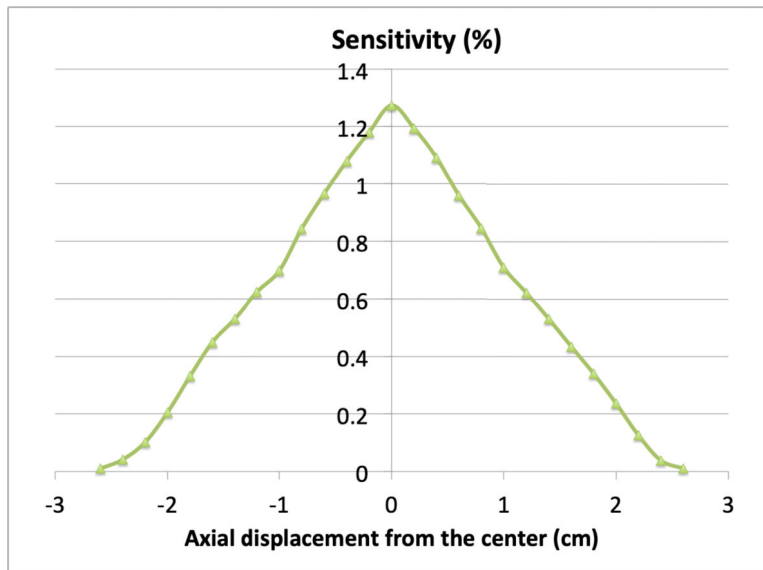
Fig. 5.
Sensitivity profile of the scanner measured with 350 to 700 keV energy window.
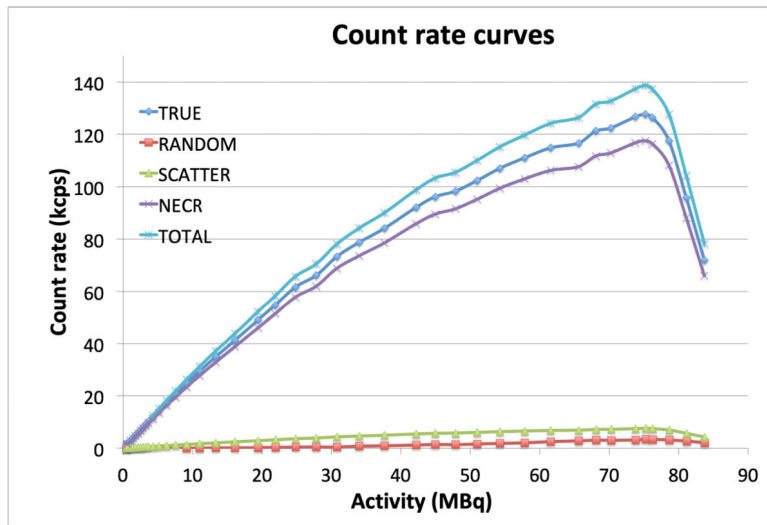
Fig. 6.
Counting rate curves of the prototype scanner measured with NEMA NU-4 "rat" phantom.
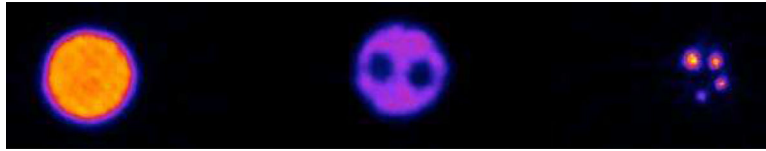
Fig. 7.
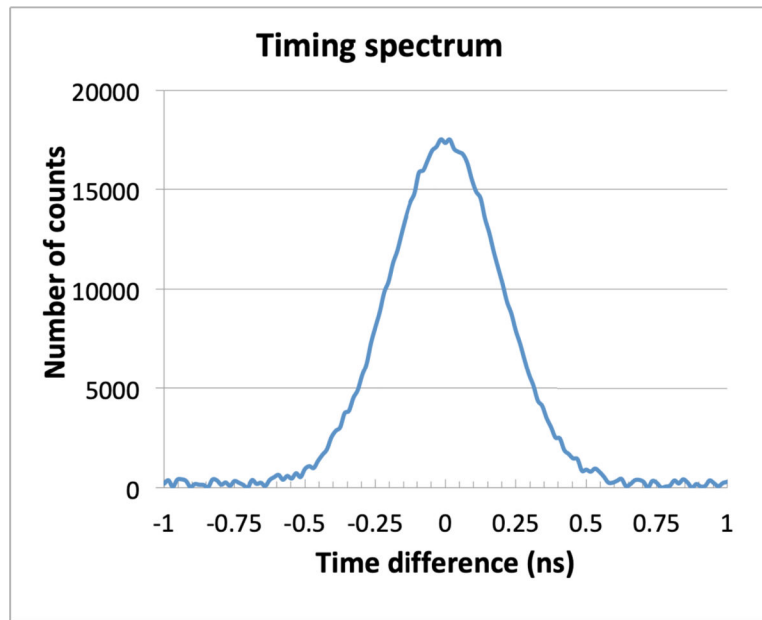Single slices through the three regions of NEMA QA phantom.
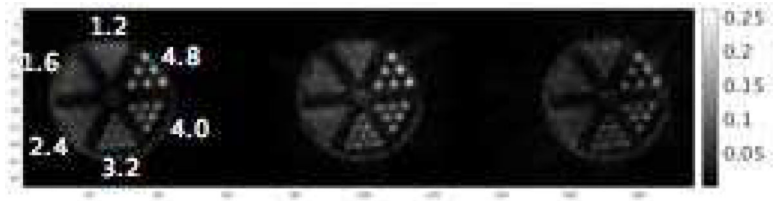
Fig. 8.
Timing resolution of the scanner.

Fig. 9.
Single slices through a Derenzo resolution phantom. Images were reconstructed with no TOF (left), with 280 ps (center) and 460 ps (right) kernels.
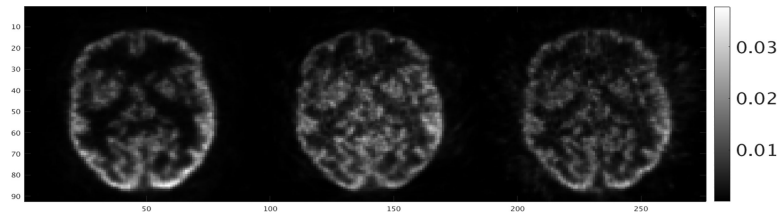
Fig. 10.
Single slices through Hoffman brain phantom. Images were reconstructed with no TOF (left) kernel, with 280 ps (center) and 460 ps (right) kernels.